Using DInSAR to Separate Surface and Subsurface Features

Keith Morrison, *Member, IEEE*, John C. Bennett, and Matt Nolan

***Abstract*—We report on an investigation into the use of differential interferometric synthetic aperture radar (SAR) (DInSAR) for the discrimination between surface and subsurface features in a soil, undertaken at the Ground-Based SAR Microwave Measurement Facility. A temporal sequence of C-band VV SAR images of a drying soil containing a buried target was collected. While the phase record of the signal identified with the soil return showed almost no variation, in stark contrast, the phase from the buried target showed a strongly linear change with time. A model is presented, which describes the observed phase changes in terms of retardation of the signal by the soil dielectric properties, which are dependent upon the moisture content. The model confirms a strongly linear relationship between phase and volumetric soil moisture. The linearity promises to greatly simplify any exploitation scheme, and such a DInSAR scheme would be applicable at large standoff distances from airborne and spaceborne platforms, in contrast to current subsurface techniques which rely on close-in measurement to spatially isolate returns vertically in backscatter.**

***Index Terms*—Dielectric materials, ground-penetrating radar, moisture measurement, permittivity measurement, radar imaging, radar signal analysis, radar signature, soil measurements, synthetic aperture imaging, synthetic aperture radar (SAR).**

I. Introduction

SYNTHETIC aperture radar (SAR) is the main imaging tool for airborne and spaceborne radar platforms and allows rapid repeat imaging of large parts of the Earth's surface. While it can provide high-resolution discrimination in angle and range, it is ambiguous in the vertical direction, providing no height information in a scene. As a consequence, schemes for discriminating between surface and buried features have relied on ground-based systems [1]–[4] or low-flying nadir-looking aerial platforms [5]–[7] with sufficiently high resolution to be able to separate features vertically. The use of ground-based systems, in particular, places severe restrictions on the size of the area that can be investigated or accessed.

Manuscript received July 31, 2010; revised August 26, 2011 and April 19, 2012; accepted September 16, 2012. Date of publication December 12, 2012; date of current version May 16, 2013. This work was supported by the U.S. Department of Defense, through the Army Research Laboratory's Defense Experimental Program to Stimulate Competitive Research (DEPSCOR) Program.

K. Morrison is with the Department of Informatics and Systems Engineering, Cranfield University, SN6 8LA Shrivenham, U.K. (e-mail: k.morrison@cranfield.ac.uk).

J. C. Bennett was with the Department of Electronic and Electrical Engineering, The University of Sheffield, S1 3JD Sheffield, U.K. He resides near Sheffield, U.K. (e-mail: j.c.bennett@sheffield.ac.uk).

M. Nolan is with the Institute of Northern Engineering, University of Alaska—Fairbanks, Fairbanks, AK 99775-5910 USA (e-mail: matt.nolan@uaf.edu).

Digital Object Identifier 10.1109/TGRS.2012.2226183

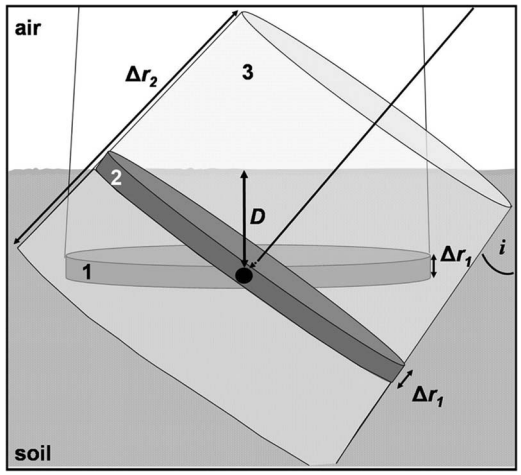

Fig. 1. Schematic to demonstrate the problem of range layover between surface and subsurface returns. The buried feature is shown as a black sphere at a depth D. Nadir-looking beam **1** has good slant range resolution (labeled as Δr_1), sufficient to isolate the buried feature from the surface return in the vertical direction. For the same beam tilted off nadir (beam **2**), as the signal back at the radar is an integration of all returns within the volume defined by the area of the beam footprint and Δr_1, it is ambiguous in height through the soil volume and surface. Beam **3** demonstrates the case of a beam with insufficient slant range (Δr_2) or beamwidth resolution to provide separation of the buried feature or surface returns. Beams **1** and **2** are illustrative of a ground-based UWB radar, and beam **3** is illustrative of an airborne or spaceborne SAR.

Fig. 1 shows the illumination of a soil volume for three scenarios. While a nadir-pointing ground-based ultrawideband (UWB) radar can obtain high (vertical) range resolution, off nadir, the surface and subsurface returns are no longer separable, placing severe restrictions on any side-looking wide-area airborne imaging application. The problem of surface-clutter separation increases with distance from the target, a problem exemplified by satellite radar altimeters [8]. Fig. 1 also shows the case for an airborne or spaceborne SAR where a smaller bandwidth has exacerbated surface and subsurface layover. As such, standoff airborne (other than very low flying) and spaceborne systems are unable to provide separation of surface and subsurface features with current detection schemes based on their isolation in backscatter.

Across-track interferometric SAR (InSAR) uses phase measurements of the same scene from two slightly different perspectives to estimate height at each point in the scene [9]. The accuracy of the technique varies with imaging geometry, radar parameters, and target characteristics. From space, absolute vertical accuracies on the order of tens of wavelengths are possible, while from airborne platforms, accuracies approaching a wavelength are possible [10], [11]. However, while providing a

height estimate at a point, it would still not be able to discriminate between a surface and a subsurface return. Differential InSAR (DInSAR) uses a temporal sequence of repeat images to obtain a very accurate record of phase change, potentially providing subwavelength measurement accuracy. The first image pair provides the topography of the scene, which provides the reference surface against which successive images are measured. Subsequent phase changes are directly interpreted as changes in the radial path length between an image point and the radar [12]–[14].

DInSAR changes have traditionally been interpreted as surface deformation over a soil. However, this work reports on a laboratory investigation into the phase behavior of a soil-buried target across a set of DInSAR images to investigate whether phase can be used as a discriminant between surface and subsurface features in a SAR scene. A varying soil moisture was seen to differentially affect the phase histories of the surface and subsurface signals, allowing unambiguous separation of the returns. Such a scheme could be exploited at large standoff distances, applicable to airborne and spaceborne platforms. A model is presented to explain the experimental results.

II. Laboratory Measurement

A program of experimental work was undertaken at the indoor Ground-Based SAR Microwave Measurement Facility [15]–[17]. This is a 6 m $(l) \times 4$ m $(w) \times 3$ m (h) anechoic chamber, which provides a highly controlled radar measurement environment. A temporal sequence of high-resolution C-band SAR imagery of a drying soil sample containing a buried target was obtained.

A. Soil Sample

The soil sample was composed of 100% fine "smooth" sand, of the type used in cement mortar, and with a dry-weight density of 1.602 g/cm^3. It had an area of 88 cm $\times$ 195 cm and a mean depth of 20.5 cm, providing a total volume of 0.35 m^3. It was part of a larger 176 cm $\times$ 195 cm soil sample, but the other half was not used in this experiment. The sample was locked in position to ensure that no movement disturbance occurred to the sample during the experiment. For study purposes, the sample was divided up into two halves of equal area of 88 cm $\times$ 97.5 cm. A trihedral was buried near the center of each area with its apex approximately at half the soil depth, each angled to present the maximum radar cross section toward the radar. The soil was then raked during infilling to provide homogeneity across and through the sample and top brushed to provide a smooth surface. The preexisting volumetric water content within the sample was estimated to be very low at below 2%. As evenly as possible, 0.86 L of water was added to Area 1 from a handheld watering can with a rose dispenser. Area 2 was left dry during the experiment. Fig. 2 shows the soil sample shortly after completion of the measurements, showing a clear delineation between Area 1 and Area 2. To reduce unwanted radar clutter from the soil container and support, the long edge of the sample was turned through 45° relative to the SAR scan direction, such that the sample corners were aligned in the range and cross-range directions. Fig. 3 shows the postmeasurement excavation of the soil visible in Area 1, indicating that the water penetrated down to a depth of 1.5 cm. With knowledge of the volume of water added and ignoring any initial moisture present in the sand, we can estimate the volumetric water content (a dimensionless fraction representing the ratio of water volume to soil volume) as $m_v = 0.067$ within the 1.5-cm wet layer.

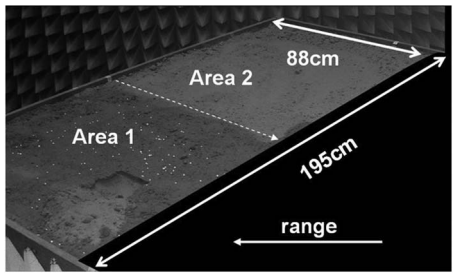

Fig. 2. Photograph of the soil sample after completion of the experiment and showing a small excavation pit for investigation of water penetration. The sample was oriented at 45° to the principal SAR imaging axes to reduce clutter from the container and supporting structure. 0.86 L of water was added to Area 1, while Area 2 was left dry. A -3-dB $\cdot$ m^2 trihedral was buried at a depth of 10 cm in Area 1, and a -10-dB $\cdot$ m^2 trihedral was buried at a depth of 12 cm in Area 2. The polystyrene markers described in Section II-C are visible in Area 1.

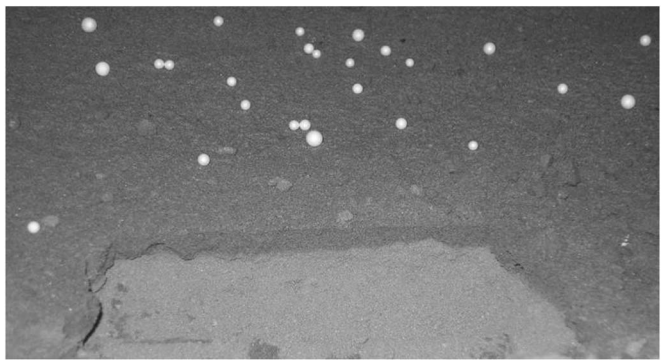

Fig. 3. Zoomed view of the excavation pit visible in Area 1 in Fig. 2. There was a clear boundary between the 1.5-cm-thick wet top layer and the underlying dry zone. The polystyrene markers described in Section II-C are clearly visible.

B. SAR Imaging

A series of SAR images of the soil sample was taken. The antenna was positioned 200 cm above the soil surface, and the sample was displaced in the range direction such that the central point of the sample on the border between Area 1 and Area 2 was at a ground range of 250 cm. The C-band VV measurements used a microwave RF subsystem based around an HP8720DX vector network analyzer. The spacing of the samples along the aperture dx was set at 1.5 cm $(\lambda/4)$ so as to avoid grating lobes. During imaging, the antenna stopped at each sample point along the aperture, stepped through a set of 401 spot frequencies at 5-MHz intervals over a 4–6-GHz bandwidth, then moved on dx, and repeated the process until 77 samples had been collected over a 114-cm aperture. Thus, an image is not collected instantaneously but takes 1.5 min, during which time RF and mechanical stability of the radar and target must be maintained. The range and cross-range resolutions vary

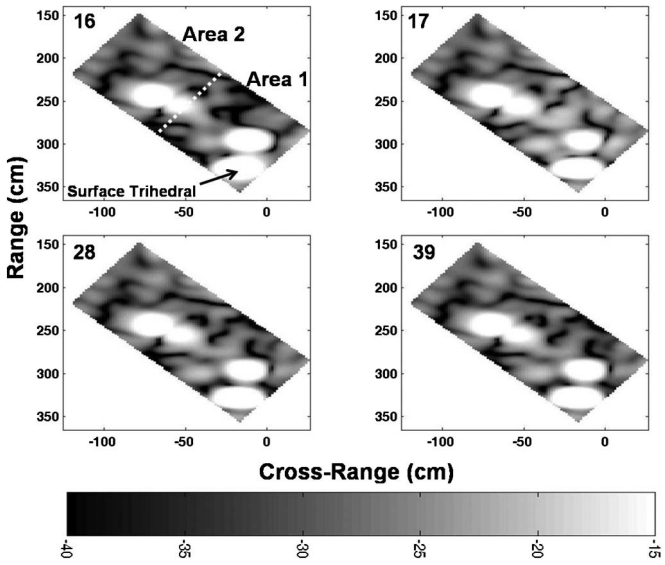

Fig. 4. Four SAR images of the sample. The dashed line in the top left image delineates Area 1 and Area 2. A surface-mounted reference trihedral placed at the far-range apex of Area 1 is indicated. The bright feature just in front is the buried trihedral. The dominant feature in Area 2 is the buried trihedral (the bright feature immediately to its right probably arises from an interaction with the box base). Image 16 shows the sample just prior to addition of water to Area 1, image 17 shows the sample at $T = 10$, i.e., 10 min after addition of the water, image 28 is for $T = 138$, and image 39 shows the final measurement at $T = 249$. The imagery is presented over a 25-dB dynamic range. Each was first prepared over a 40-dB range, normalized to 0 dB relative to the reference trihedral (the strongest feature) in the first image. To better show the weaker features, each is only presented over the range of -15 to -40 dB. The image pixel size is 1.5 cm $\times$ 1.5 cm.

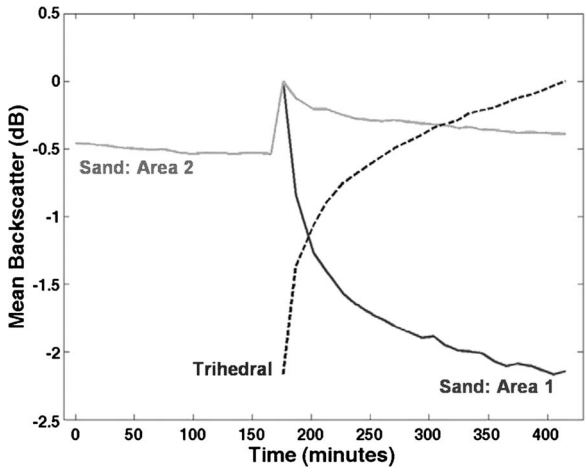

Fig. 5. Temporal variation of backscatter during the experiment. The light solid line shows the soil return from Area 2 during the entirety of the experiment. The addition of water at 167 min is evident in the 0.5-dB jump caused by some leakage into Area 2 from Area 1. The dark solid line shows the change in the soil backscatter from Area 1 after addition of the water, and the dashed line shows that from the buried trihedral in Area 1. The soil backscatter curves have both been set to 0 dB at the first "wet" measurement (image 17), while the final trihedral return was also set to this value (image 39). In addition, the trihedral curve has been shifted down 11 dB for easier display.

across the sample but were typically 10 cm in both directions. An initial sequence of 16 SAR images of the sample prior to addition of water was first acquired over a 2.75-h interval. This was to allow any settlement in the soil resulting from the disturbance from the sample preparation and to confirm the radiometric stability of the measurement system. Water was added to Area 1; then, a sequence of further 23 images begun 10 min later for a 4-h period. The mean interval between images was just under 11 min. Stringent calibration and stability procedures were required for the radar measurements and have already been described in greater detail elsewhere [15], [18].

A synthetic-pulse plane-to-plane imaging scheme was used to construct the time series of SAR images [19]. Fig. 4 shows a sequence of four SAR images of the soil during the experiment. The first shows the sample just prior to addition of the water (image 16). The trihedrals are clearly visible as dominant features in each area, and because the SAR imaging plane is at the soil surface, they exhibit range layover and appear further downrange of their actual positions. The bright feature at the far range of Area 1 is a reference trihedral placed on the sand surface at the back apex of the sample. The next three images show the first "wet" image 10 min after addition of the water to Area 1 (image 17), the image midway at 138 min (image 28), and the final image at 249 min (image 39).

C. Optical Imaging

In order to correctly interpret the radar measurements, it was necessary to optically monitor the sample for any physical movement of the surface horizon during the experiment. For this purpose, high-resolution (2448 $\times$ 3264 pixels) digital color photographs of the soil were acquired using an Olympus SP-350 digital camera. It was installed on the rear of the sample at a shallow viewing angle, sufficiently distant from the sample so as to cause no contamination to the measurements. A time-lapse series of optical images of the soil at 5-min intervals was recorded during the course of the experiment. Because of the low contrast and the lack of discernible features over the soil surface, markers were added, which could more easily be tracked. Polystyrene balls approximately 4 mm in diameter were scattered over the surface of Area 1 after watering to act as reference features and are evident in Figs. 2 and 3. These were sufficiently light so as to move with the soil surface, small enough not to cause any local soil moisture effects, and invisible to the radar. A more detailed discussion of the processing has already been given in [18]. Examination of the optical imagery indicated that the physical soil surface was static down to a vertical measurement accuracy of 0.1 mm, in agreement with previous characterization of this soil sample [18]. This corresponds to a maximum possible phase contribution of only 1.2° to the results and can be ignored for analysis purposes.

III. Results

A. Amplitude Behavior

Fig. 4 indicates that the buried trihedral in Area 1 showed a clear reduction in backscatter with the addition of water, which increased thereafter. Fig. 5 shows the variation in mean soil backscatter from Area 1 and Area 2 (both excluding the trihedral regions) and from the buried trihedral in Area 1. The return from Area 2, which acted as the control, shows that the measurement stability was 0.1 dB over the first 166 min of the experiment. The 0.5-dB jump is associated with some slight

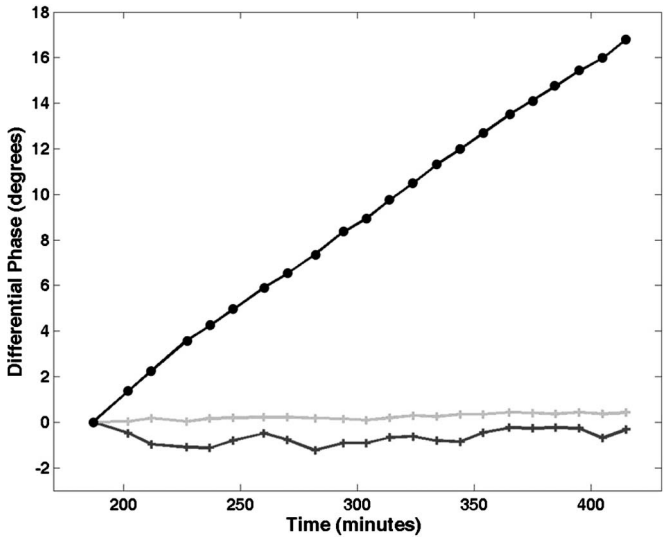

Fig. 6. Phase changes observed at the (dark circle line) buried trihedral in Area 1 and the (dark tick line) soil in Area 1 following addition of water (images 18–39). For reference, the (light tick line) return from the buried trihedral in Area 2 is also shown.

contamination of Area 2 along its border with Area 1 at the addition of the water. The subsequent fall in the backscatter is largely attributed to drying from the contaminated region. The change in mean backscatter from Area 1 after addition of the water showed a 2.15-dB drop over the subsequent 239 min. The increase in trihedral strength inversely mirrors the backscatter curve of the soil return, indicating that the reducing reflectivity of the soil provided a matched increase in transmission through the soil medium to the trihedral.

B. Phase Behavior

Using the first "wet" image as the master I_{17}, a series of complex differential interferograms IF_{17_N} was constructed by reference against successive images I_N pixel by pixel

$$\mathrm{IF}_{17\_N} = \mathrm{angle}\left\{I_{17} \cdot I_N^*\right\} \tag{1}$$

where $N = 18{-}39$ and the asterisk superscript represents conjugation. Fig. 6 shows the differential phase behavior of the soil and the buried trihedral in Area 1. Also shown for reference is the phase behavior from the buried trihedral in unwetted Area 2. There is a striking difference in behavior between the surface and buried trihedral returns in Area 1, with the trihedral showing a strongly linear and positive phase change of $+17^\circ$. In contrast, the soil return shows very little change, with an irregular 1° oscillation in phase.

IV. Model

The experiment was set up such that the only changing variable was m_v and its distribution through the soil volume. Regarding the latter, later experiments suggest that it would have reached its maximum penetration depth (1.5 cm) within 10 min, such that we consider the vertical water distribution static over the duration of the experiment. With the optical measurements indicating a static surface, the signal passed through the same soil depth throughout the experiment to the buried target. In Fig. 7, we consider a two-layer soil representing the experimental setup. The upper 1.5-cm "wet" layer is homogeneous with respect to moisture (and hence dielectric). The lower "dry" layer contains a buried object at depth $D = 10$ cm. We initially consider the case of normal incidence ($i = 0^\circ$), such that we may ignore refraction effects. Considering a layer as a lossy medium with complex dielectric constant $\varepsilon = \varepsilon_r - j\varepsilon_i$, then propagation of a signal through a distance z is described by

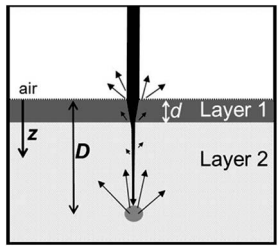

Fig. 7. Normal incidence scattering scheme for soil containing a buried object at depth D. The two-layer soil has an upper wet layer of thickness $d = 1.5$ cm and a lower dry layer which contains the buried point target at $D = 10$ cm. The soil is nonexpansive, exhibiting no shrink or swell, such that the physical surface horizon is unchanging with time. Scattering arises from discontinuities in the medium, namely, at the soil/target interface, air/soil interface, and wet/dry-soil interface. Other discontinuities may give rise to other returns from the volume. The signal suffers attenuation as it passes down through the soil, most strongly in the wet layer.

$$S(z) = \exp(-\gamma z) = \exp(-\alpha z)(-j\beta z) \tag{2}$$

where the propagation constant γ can be written as

$$\begin{aligned}\gamma &= \alpha + \beta = j\frac{2\pi}{\lambda}\sqrt{\varepsilon_r - j\varepsilon_i} \\ &= j\frac{2\pi}{\lambda}\sqrt{\varepsilon_r(1 - j\tan\delta)}\end{aligned} \tag{3}$$

where $\tan\delta = \varepsilon_i/\varepsilon_r$ and λ is the wavelength. The α term describes the attenuation through the medium, and the phase term β is given by the imaginary part in (3); thus

$$\beta = k\sqrt{\varepsilon_r}\sqrt[4]{1 + (\tan\delta)^2}\cos\left(\frac{\delta}{2}\right) \tag{4}$$

where $k = 2\pi/\lambda$ is the wavenumber. This shows that the phase change with propagation depends on the loss tangent angle as well as the real part of the dielectric constant ε_r. Between any two measurements, the phase change from the buried target will depend only upon the change in dielectric, through the variation in soil moisture Δm_v, during the experiment. Equation (14) from [20] provides quadratic expressions for ε_r and ε_i for the case of a 100% sandy soil

$$\varepsilon_r = a_0 + a_1 m_v + a_2 m_v^2 \tag{5}$$

$$\varepsilon_i = b_0 + b_1 m_v + b_2 m_v^2 \tag{6}$$

where the a and b coefficients depend upon the radar frequency. Fig. 8 shows the variation of the magnitude of the dielectric constant against m_v for the C-band 5-GHz case.

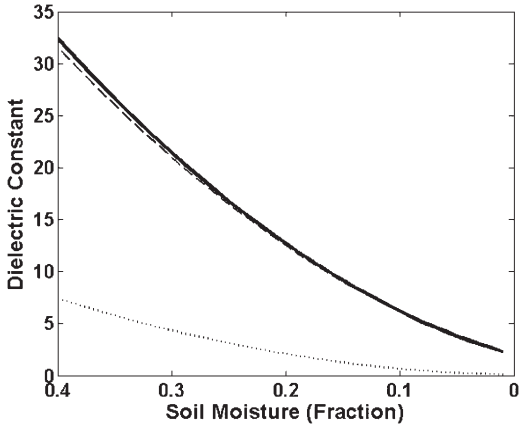

Fig. 8. (Solid line) Modeled variation of the magnitude of the dielectric constant $|\varepsilon|$ against soil moisture m_v showing its distribution between the (dashed line) real and (dotted line) imaginary components. The x-axis displays decreasing m_v left to right, representative for the case of a drying soil. The a and b coefficients in (5) and (6) were chosen to be representative of 5 GHz, such that $\varepsilon_r = 2.0 + 31.6m_v + 106.1m_v^2$ and $\varepsilon_i = 0.1 + 1.6m_v + 42.1m_v^2$.

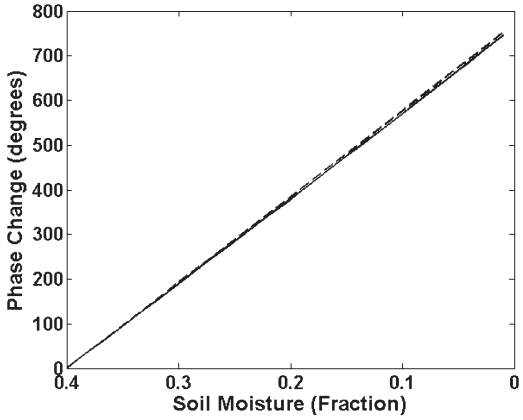

Fig. 9. Modeled phase change from the buried target in Fig. 7 due to the signal passing (two-way) through an upper 1.5-cm wet layer, as the soil moisture m_v decreases from 0.4 to 0.01. The solid line shows the phase change calculated using the exact solution given in (4). The dashed line is estimated using the approximation given in (8). A thicker layer would produce a steeper gradient.

Fig. 9 uses (4) with (5) and (6) to calculate the phase change $\Delta\phi$ for $z = 0.015$ m and a change in m_v from 0.01 to 0.4. The phase changes arise solely from the 1.5-cm-wide wet Layer 1 in Fig. 7. Dry thicker Layer 2 displays no change in m_v and therefore contributes no phase change. It is seen that the positive phase change is strongly linear over the whole m_v range considered (in the convention adopted, a positive change is indicative of decreasing distance between the radar and the target). This is understood in terms of the decreasing electrical path length from a fixed reflection point at the object's depth as the dielectric constant reduces with drying of the soil.

Fig. 8 shows that, for the case under consideration here, $\varepsilon \cong \varepsilon_r$, such that the $\tan\delta$ angle must be small. In fact, δ varies by only 11° over the $\Delta = 0.39$ range considered, such that $\cos(\delta/2) \sim 1$. Inspection of (4) shows that, with omission of the $\cos(\delta/2)$ term and multiplying the ε_r term by the $\sqrt[4]{}$ term, (4) can be rewritten in a usefully compact approximate form

$$\beta \approx k\sqrt{\varepsilon_r^2 + \varepsilon_i^2} = k\sqrt{|\varepsilon|}. \tag{7}$$

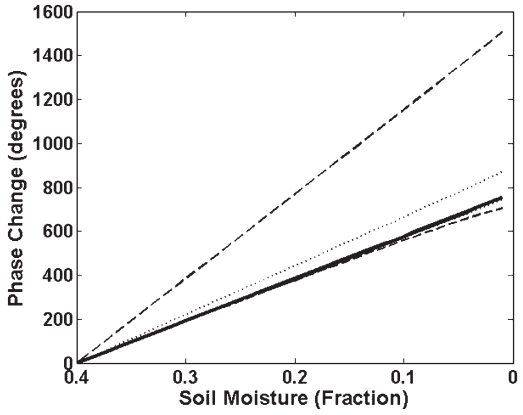

Fig. 10. Modeled variation in phase from the buried object shown in Fig. 7 for decreasing soil moisture. The thick solid line shows the normal incidence case. The dashed and dotted lines show the cases for incidence angles of 60° and 30°, respectively. For each, the upper line shows the no-refraction case, and the lower line shows the case with refraction. The difference between the two cases is most significant at the larger incidence angle. The with-refraction curves are almost coincident with the normal incidence case, particularly at higher soil moistures.

Hence, the change in phase for the two-way path is given by

$$\Delta\phi = 2kd\left\{\sqrt{|\varepsilon_m|} - \sqrt{|\varepsilon_n|}\right\} \tag{8}$$

where d is the vertical thickness of wet Layer 1 and the subscripts represent the magnitudes of the dielectric constant values at times m and n. $\Delta\phi$ is plotted in Fig. 9, which shows that it almost lies on top of the phase derived without approximation from (4).

A. Incidence Angle and Refraction Effects

For the more general case of incidence angles away from 0°, we first convert the layer thickness z to a slant thickness. In the absence of refraction at the air/soil boundary, this would be accomplished by inclusion of a $1/\cos i$ term into (8); thus

$$\Delta\phi = \frac{2kd}{\cos i}\left\{\sqrt{|\varepsilon_m|} - \sqrt{|\varepsilon_n|}\right\}. \tag{9}$$

With the need to include refraction, the final form of the equation is

$$\Delta\phi = \frac{2kd}{\cos i}\left\{\frac{\sqrt{|\varepsilon_m|}}{\cos t_m} - \frac{\sqrt{|\varepsilon_n|}}{\cos t_n}\right\} \tag{10}$$

where t is the angle of transmission of the ray into the soil. The transmission angle is related to the incidence angle via Snell's law

$$t = \sin^{-1}\left[\frac{\sin i}{\sqrt{|\varepsilon|}}\right]. \tag{11}$$

Fig. 10 shows the results from (9) and (10) for the $i = 30^\circ$ and 60° cases, i.e., for the off-normal cases ignoring refraction and inclusive of refraction. All produce a strongly linear relationship between soil moisture and phase change. It is seen that refraction reduces the size of the phase change relative to the no-refraction case, due to bending of the ray toward the normal, reducing the apparent slant depth of the layer. The difference is

angle dependent, reducing the phase changes by 15% and 50% for the $i = 30^\circ$ and 60° cases, respectively. What is perhaps surprising is that the refracted waves for the 30° and 60° cases lie almost on top of each other. In addition, Fig. 10 shows that these lie very close to the $i = 0$ case. Thus, the behavior of the off-normal refracted signal is very close to that of a normal incidence ray, independent of the actual incidence angle that the scene is viewed at. This is a very useful simplification, negating the need to consider refraction effects, which might otherwise require knowledge of soil dielectric values. Adopting the normal incidence line from Fig. 10, the measured phase change of 17° would indicate a change in m_v of 0.0034 or a 5% reduction from the initial moisture content over the course of the experiment. From previous knowledge of soil drying rates in the measurement laboratory, this is an entirely reasonable estimate.

V. Comment

The aforementioned work indicated that the surface signal from a drying soil was distinguishable from that arising from a buried target by examination of their respective phase signatures. The former displayed almost no variation, while the latter showed a clear linear phase change with time. The surface response can be understood if the dominant return occurs at the air/soil interface, which was unchanging during the experiment. A much weaker volume return may also have been present, likely arising at the wet/dry interface boundary, which was not significant to perturb the surface return. The buried target phase history could be understood as due to the decreasing retardation of the signal through the wet layer as it began to dry out.

While the laboratory work was limited, the interpretation of the result is supported by the modeling results. In agreement with experiment, the model predicts a phase history linear with changing soil moisture. Soils can be expected to have varying degrees of heterogeneity in the vertical distribution of moisture. The phase modeling scheme predicts that it does not matter how any moisture is distributed in the soil; it is only the total "bulk" moisture (dielectric) change in the soil column above the target that has an effect on the phase history.

The discrimination scheme would seem to have a practical use in SAR image analysis. Just as InSAR and DInSAR use phase to extract height and displacement information at much greater resolution than is present in the component backscatter images, so too this scheme can discriminate at the subresolution scale. In consideration of a vertically dispersed group of objects within a resolution voxel, the phase response will be a summation of the set of linear phase terms, and it may be possible to spectrally unmix the individual object returns using Fourier and related techniques. As the scheme operates on phase rather than backscatter, it can be applied at large standoff distances from airborne and spaceborne platforms. This would provide an opportunity to dramatically increase the size of areas that could be surveyed in the detection of buried mines and unexploded ordnance. Buried archaeological features might also reveal themselves in the same way. Because of the strong link between phase and soil moisture, it should also be possible to exploit this to measure soil moisture with the use of buried reference targets.

The first discriminant of buried features would be backscatter features over a soil that consistently display large phase changes relative to other pixels. If the direction of change of soil moisture is known between measurements, the sign of the phase change will track this. For those pixels with the appropriate phase behavior and therefore suspected of association with buried features, a second discriminant is the backscatter behavior. The direction of change should run counter to the signature of surface return pixels. Increasing backscatter for decreasing moisture is likely indicative of the signature of a buried feature. As the application of any scheme can expect to be complicated and compromised by the complexity of the real world, the availability of two discriminants to reduce false positives is important.

The proposed scheme is limited in terms of radar platform, soil type, terrain, and moisture range. It requires the target return to be stronger than the integrated return from the overlying soil column and clutter elsewhere within the voxel. Because the penetration depths are modest at the most commonly used L-, C-, and X-band remote sensing frequencies, targets will likely only be visible for relatively small moisture contents. These considerations indicate an application most suited toward arid regions, although low rainfall rates may significantly reduce the time when suitable moisture conditions are present. A challenge would be to provide sufficiently short sampling intervals which can capture fully the patterns of variation.

References

[1] Y. Sun and J. Li, "Time–frequency analysis for plastic landmine detection via forward-looking ground penetrating radar," *Proc. Inst. Elect. Eng.—Radar Sonar Navig.*, vol. 150, no. 4, pp. 253–261, Aug. 2003.

[2] L. Carin, N. Geng, and M. McClure, "Ultra-wide-band synthetic aperture radar for mine-field detection," *IEEE Antennas Propag. Mag.*, vol. 41, no. 1, pp. 18–33, Feb. 1999.

[3] C. Leuschen, N. Goodman, C. Allen, and R. Plumb, "An interferometric technique for synthetic aperture ground-penetrating radar," in *Proc. IGARSS*, Lincoln, NE, May 27–31, 1996, vol. 4, pp. 2033–2035.

[4] P. van Genderen and I. Nicolaescu, "System description of a stepped frequency CW radar for humanitarian demining," in *Proc. 2nd Int. Workshop Adv. GPR*, Delft, The Netherlands, May 14–16, 2003, pp. 9–15.

[5] A. Fijany, J. B. Collier, and A. Citak, "Recent advances in unexploded ordnance detection (UXO) using airborne ground penetrating SAR," in *Proc. Aerosp. Conf.*, 1999, vol. 3, pp. 429–441.

[6] F. Fruehauf, A. Heilig, M. Schneebeli, W. Fellin, and O. Scherzer, "Experiments and algorithms to detect snow avalanche victims using airborne ground-penetrating radar," *IEEE Trans. Geosci. Remote Sens.*, vol. 47, no. 7, pp. 2240–2251, Jul. 2009.

[7] Kosovo Trials Report. [Online]. Available: http://www.mineseeker.org

[8] F. T. Ulaby, R. K. Moore, and A. K. Fung, *Microwave Remote Sensing*, vol. I. Reading, MA: Addison-Wesley, 1982.

[9] R. Bamler and P. Hartl, "Synthetic aperture radar interferometry," *Inverse Probl.*, vol. 14, no. 4, pp. R1–R54, Aug. 1998.

[10] L. Jie, H. Haifeng, and L. Diannong, "Height-measure accuracy analysis of distributed spaceborne InSAR system," in *Proc. APSAR*, Nov. 5–9, 2007, pp. 650–654.

[11] J. Moreira, "Design of an airborne interferometric SAR for high precision DEM generation," *Int. Archives of Photogramm. Remote Sens.*, vol. XXXI, pt. B2, pp. 256–260, 1996.

[12] H. A. Zebker, P. Rosen, and R. Goldstein, "On the derivation of coseismic displacement fields using differential radar interferometry: The Landers earthquake," *J. Geophys. Res.*, vol. 99, no. B10, pp. 19 617–19 634, 1994.

[13] A. Ferretti, G. Savio, R. Barzaghi, A. Borghi, S. Musazzi, F. Novali, C. Prati, and F. Rocca, "Submillimeter accuracy of InSAR time series: Experimental validation," *IEEE Trans. Geosci. Remote Sens.*, vol. 45, no. 5, pp. 1142–1153, May 2007.

[14] D. Massonnet and K. Feigl, "Radar interferometry and its application to changes in the earth's surface," *Rev. Geophys.*, vol. 36, no. 4, pp. 441–500, Nov. 1998.
[15] K. Morrison, J. C. Bennett, G. Cookmartin, A. J. McDonald, and S. Quegan, "Three-dimensional X-band SAR imaging of a small conifer tree," *Int. J. Remote Sens.*, vol. 22, no. 4, pp. 705–710, Mar. 2001.
[16] S. C. M. Brown, S. Quegan, K. Morrison, J. C. Bennett, and G. Cookmartin, "High resolution measurements of scattering in wheat canopies—Implications for crop retrieval," *IEEE Trans. Geosci. Remote Sens.*, vol. 41, no. 7, pp. 1602–1610, Jul. 2003.
[17] K. Morrison, J. C. Bennett, G. Cookmartin, S. Quegan, and A. Race, "Development and capabilities of the ground-based SAR (GB-SAR) facility," in *Proc. Adv. SAR Workshop*, Montreal, QC, Canada, Jun. 25–26, 2003, [CD-ROM].
[18] K. Morrison, J. C. Bennett, M. Nolan, and R. Menon, "Laboratory measurement of the DInSAR response to spatio-temporal variations in soil moisture," *IEEE Trans. Geosci. Remote Sens.*, vol. 49, no. 10, pp. 3815–3823, Oct. 2011.
[19] J. W. Goodman, *Introduction to Fourier Optics*. New York: McGraw-Hill, 1968.
[20] M. T. Hallikainen, F. T. Ulaby, M. C. Dobson, and M. A. El-Rayes, "Microwave dielectric behavior of wet soil—Part 1: Empirical models and experimental observations," *IEEE Trans. Geosci. Remote Sens.*, vol. GE-23, no. 1, pp. 25–34, Jan. 1985.

Keith Morrison (M'96) received the B.Sc. degree in physics with astrophysics from the University of Leicester, Leicester, U.K., in 1983 and the Ph.D. degree in astronomy and astrophysics from the University of St Andrews, St Andrews, U.K., in 1987.

He was with the British Antarctic Survey, Cambridge, U.K. in 1987–1994, The University of Sheffield, Sheffield, U.K., in 1994–2000, and QinetiQ, Malvern, U.K., in 2000–2002. Since 2002, he has been with Cranfield University, Shrivenham, U.K. His main research interest is the development and application of ground-based synthetic aperture radar imaging and signal processing techniques applied to environmental remote sensing.

John C. Bennett received the B.Eng. and Ph.D. degrees in electronic engineering from The University of Sheffield, Sheffield, U.K., in 1970 and 1974, respectively.

He is currently a Consultant, having retired from his post as Reader at The University of Sheffield. He is currently involved in the use of both laboratory and outdoor ground-based synthetic aperture radar systems for radar cross section measurements. He has previously been involved with the microwave metrology of reflector antennas and with antenna near-/far-field transformation techniques.

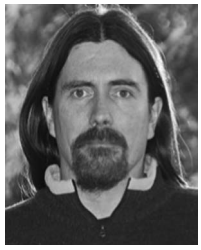

Matt Nolan received the B.S. degree in mechanical engineering from Carnegie Mellon University, Pittsburgh, PA, in 1988, the M.S. degree in Arctic engineering from The University of Alaska, Anchorage, in 1992, and the Ph.D. degree in geophysics from The University of Alaska, Fairbanks, in 1998.

He is currently a Research Associate Professor with The University of Alaska, Fairbanks. His primary research interests include glaciers, permafrost, and climate in the Arctic, using field and remote sensing techniques.